Buckling Mechanics Modulus Measurement of Anisotropic Cellulose Nanocrystal Thin Films

Nolan A. Miller^{a1}, Zhaofan Li^b, Wenjie Xia^b, Chelsea S. Davis^{a*}

- ^a School of Materials Engineering, Purdue University, West Lafayette, Indiana 47907
- Department of Civil, Construction, and Environmental Engineering, North Dakota State
 University, Fargo, North Dakota 58108
- *Corresponding Author: Email address: chelsea@purdue.edu (C.S.D.)
- ¹Present Address: School of Polymer Science & Engineering, University of Massachusetts
 Amherst, Amherst, Massachusetts 01003

Keywords:

Cellulose nanocrystals, particle assembly mechanics, modulus, thin film mechanics, surface buckling, wrinkling, anisotropy

Abstract

Bio-derived materials have become an increasingly desirable alternative to materials sourced from nonrenewable resources. Cellulose nanocrystals (CNCs), often derived from wood pulp, can be used to manufacture thin films with applications ranging from optical, protective, and aesthetic coatings to sensors and batteries. Quantifying the mechanical properties of CNC films is a necessary step towards improving the quality of these bio-derived films. Because CNCs are highly anisotropic and can subsequently form highly ordered, aligned structures, an experimental method that can succinctly determine how film properties change with particle orientation is of interest. Here, spin coating an aqueous solution of CNCs onto a silicone elastomer results in a radially

aligned particle assembly. As the local orientation of these aligned, high aspect ratio particles changes with respect to a uniaxially applied compression, the mechanical response of the particle assembly was observed to vary significantly. By applying a lateral compression to a radially aligned CNC film/elastomer bilayer, surface buckles aligned orthogonal to the compression direction were observed. The wavelength of these wrinkles, coupled with the thickness of the film and the modulus of the substrate, is dictated by the modulus of the film. The modulus as a function of local CNC alignment and position for each film was thus determined in a single experiment. These experiments measured a higher modulus for the film where the orientation of the CNC particles is aligned parallel to the uniaxial compression direction. Coarse-grained modeling of closely packed, high aspect ratio particle assemblies supporting the experimental results agrees with the observed trend. By characterizing the mechanical properties of CNC films, these green materials can be further developed for industrial-scale implementation; additionally, an experimental method is proposed for concisely capturing a range of modulus values in an anisotropic particle film.

1. Introduction

The study of nanoparticle assemblies has been an increasingly attractive field of research for its potential to enable the design functional materials on multiple length scales.^[1] Cellulose nanocrystals (CNCs) are bio-derived nanoparticles that have been proposed for applications such as optical sensors, barrier coatings, structural colorants, and functionalized surfaces.^[2–6] Furthermore, these applications can be advanced with more control of the distribution, shape, and orientation of nanoparticle systems.^[3]

CNCs are a renewable resource derived via acid hydrolysis from plants, like trees and grasses, bacteria, and certain animals such as tunicates.^[1,7] Their environmentally-friendly

sourcing makes these particles a promising candidate to replace products derived from nonrenewable resources. A single CNC rod has dimensions of 3 nm to 5 nm in width and thickness and 50 nm to 500 nm in length.^[8] CNCs also exhibit anisotropic properties due to highly oriented crystalline polymer chains.^[9,10] Due to the surface chemistry and shape of the particles, CNCs have the potential to form films of oriented particles with controllable ordering.^[11] These films can replace conventional thermoplastics for applications such as protective coatings on fabrics,^[12] transparent barrier films, or commercial printing labels.^[7] However, before CNC films can be employed for these applications, the film properties must first be characterized.

While some literature describes the modulus of individual CNCs,^[7,9] the modulus and anisotropy of CNC ultrathin films (taken here to have thicknesses below 1 micrometer) have yet to be fully characterized. Reising, et al. measured the modulus of the axial and transverse direction of a thick CNC film to be approximately 30 GPa and 7 GPa, respectively, in uniaxial tensile experiments.^[13] Further, a buckling-based approach for measuring the modulus of glassy films has been used to characterize rigid isotropic CNC films and CNC composite films supported on an elastic substrate.^[14,15] This buckling approach utilizes the geometry of the specimen and substrate modulus to resolve the modulus of the thin film.^[16,17] While the chiral nematic structure adopted by CNCs during self-assembly has remained an obstacle to mechanical testing of isotropically oriented, neat thin films,^[18] our experimental method aligns the particles for improved characterization of rod-like particle assemblies. Here, we utilize this buckling technique and careful CNC film casting methods to quantify the modulus of CNC thin films aligned in the transverse and axial directions within a single experiment.

Using strain-induced elastic buckling instability for mechanical measurements (SIEBIMM)^[17] and a methodology to deposit a radially aligned CNC thin film, a substantial

amount of data can be collected from a single experiment. The buckling wavelength (λ) observed when a critical compressive strain is applied to a thin rigid film on an elastic substrate is determined by the plain strain moduli of the film and substrate (\overline{E}_f , \overline{E}_s) and the thickness of the film (t) as shown in Equation (1).

$$\lambda = 2\pi t \left(\frac{\overline{E}_f}{3\overline{E}_s}\right)^{\frac{1}{3}}$$
 Equation (1)

Whereas self-assembled CNC thin films formed via evaporation exhibit the "coffee-ring" effect,^[19] a spin coater is utilized here to induce a rapid evaporation by imparting a radial shear force to an aqueous suspension, mitigating differences in film thickness across the film.^[20] With a constant CNC film thickness, this experimental approach utilizes the wavelength of the wrinkles formed just beyond the critical wrinkling strain. The critical wrinkling strain is also dependent on film and substrate moduli as for Equation (1) but independent of the film thickness.^[21]

$$\varepsilon_w = \frac{1}{4} \left(\frac{\overline{3E}_s}{\overline{E}_f}\right)^{\frac{2}{3}}$$
 Equation (2)

Our methodology correlates the effects of the CNC film thickness, particle orientation, and degree of particle alignment to the Young's Modulus. Particle orientation is defined here as the angle between the principle compressive strain direction and the average axial direction of the CNC particles (the direction in which the CNCs are "pointing"). The degree of alignment describes how well aligned the particles are with one another in a given direction. This procedure demonstrates the ability to control the particle orientation of high aspect ratio particles within the thin film, which is useful for optical and selective barrier coating applications. [4] The experimental results are corroborated by coarse-grained (CG) modeling results that calculated the modulus of assemblies of rigid rods with varying degrees of alignment.

2. Methods

2.1 Substrate Preparation

Polydimethylsiloxane (PDMS, Dow Sylgard 184) was selected for the substrate due to its nearly linear elastic mechanical response at small strains and ease of handling. [22] The substrate was prepared by mixing the base and curing agent at a 15:1 ratio by mass. The uncured mixture was placed under vacuum for 600 s to remove trapped air bubbles. The PDMS was cured at 70 °C for 20 h in a custom glass and aluminum foil mold. The larger piece of cured PDMS was removed from the mold and cut with a razor blade into square substrates with lateral dimensions of 25 mm and a thickness of 7.4 mm. The modulus of the PDMS substrate was measured directly through indentation and found to have an average of 0.96 MPa as described in detail in the Supporting Information (Figure S1).

A corona treatment was applied to the PDMS surface immediately before spin coating of the CNC film to locally oxidize the surface to increase the surface energy and wettability (as shown in static contact angle measurements in Figure S2).²³ A corona treater (BD-20AC, Electro-Technic Products) with an electrode tip (BD-20A, Electro-Technic Products) was used to oxidize the surface of each substrate. A custom cardstock stencil was centered over the PDMS substrate prior to the treatment to constrain the application area to a circular disk with a radius of 10 mm. The electrode was suspended 5 mm away from the substrate surface, which corresponds to a power of 9.8 kV. Each specimen was treated for 30 s while the substrate was slowly translated laterally to evenly treat the surface. The enhanced hydrophilicity of the corona treated PDMS gradually decreases in air due to diffusion of unreacted silanol groups at the surface of the PDMS.^[24] Due to the transitory nature of the corona treatment, the CNC films were applied to the oxidized PDMS immediately after the corona treatment (within 60 s).

2.2 Preparation of CNC suspensions and thin films

The CNCs were received from The University of Maine Process Development Center as a 12.1 wt% suspension. This suspension was further diluted to the desired concentration (2 wt% to 4 wt%) with deionized water. The CNCs were then dispersed using a vortex mixer (Thermo Fisher Scientific). A spin coater (Laurell Technologies Corporation) was used to deposit the CNC suspension onto the hydrophilic oxide layer of a freshly corona treated PDMS substrate. Each deposition was conducted with a spin acceleration of 100 rpm s⁻² up to a terminal spin velocity of 2500 rpm. The relative humidity of the environment was maintained at 50 %RH. A marker on the center of the bottom surface of the substrate was used to align the PDMS substrate with the axis of rotation of the spin coater to ensure that the deposited film with centered with the substrate and the oxide film. The entire spin coating procedure lasted for 30 s to allow for the majority of the water in the suspension to be removed. CNC film thicknesses were measured using an interferometer (Filmetrics) by spin coating 2 wt%, 3 wt%, and 4 wt% CNC suspensions onto silicon wafers using the same spin coating parameters as for the PDMS. The resultant thicknesses were 40 nm, 70 nm, and 120 nm. Mechanical properties of films were measured within 1 h of spin coating. The circular CNC film on the PDMS substrate was then prepared for microscopy by placing the sample on the uniaxial compression stage.

2.3 Optical microscopy for buckling-based modulus measurements

A compressive strain was induced on each CNC film/PDMS substrate sample using a custom-built uniaxial stage with two manual micrometers shown schematically in Figure 1a. The illustrated overview of the sample (Figure 1b) defines the radii and angles corresponding to each position on the film.

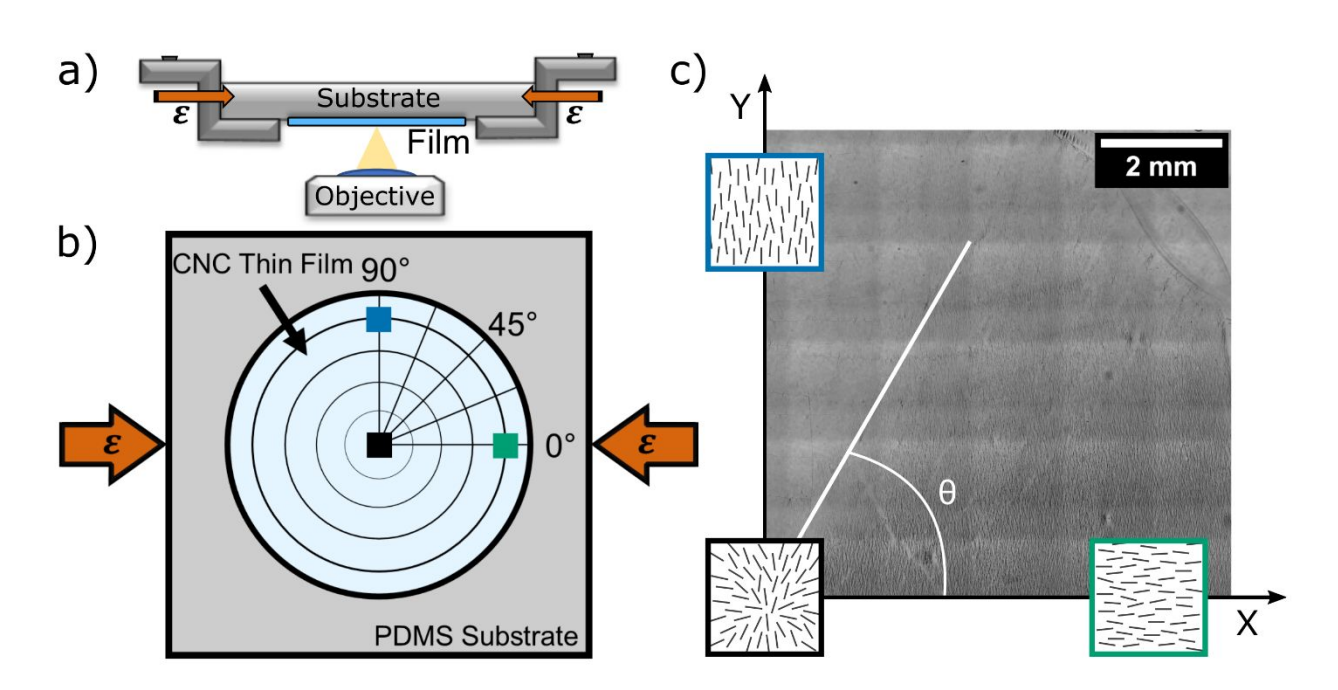


Figure 1: Experimental design (a) Mechanical stage illustrated schematically with mounted sample and micrometers applying a uniaxial compressive strain. (b) Overview of filmed substrate with annotated orientations. (c) Theoretical orientation and degree of alignment of particles as a function of radius and angle relative to the center of the film. The microscopy image depicts the first quadrant of the CNC film.

The radial shear imposed by the spin coater is expected to create a radially symmetric film of CNC particles because the axial direction of a CNC particle will align with the shear direction. Furthermore, the degree of alignment is expected to increase further from the disordered center of the film. This radial CNC particle orientation is the basis for measuring the anisotropy of the particle film.

2.4 Atomic force microscopy

Atomic force microscopy (AFM, Bruker Dimension 5000) was performed to characterize nanoscale features on the oxidized PDMS surface. A silicon nitride tip (Bruker OTR8-10, spring constant 0.57 N/m, frequency 73 kHz) was used in contact mode to measure the wrinkle wavelength of the oxide layer prior to CNC deposition. During data collection, the deflection setpoint was 0.5 V and the integral and proportional gains were set to 20 and 30, respectively.

Because the corona treatment introduces a thin oxide layer, an analogous buckling experiment was utilized to determine the thickness of only the thin oxide layer. The greater lateral resolution of the AFM was necessary to measure the small wavelengths of the wrinkled oxide layer. The thickness of the oxide layer was calculated by assuming the oxide modulus to be 70 GPa (that of SiO₂) based on the previous work of Deagen, et al. and Bowden, et al.^[25,26] The PDMS sample was compressively pre-strained 5 % and processed under the same corona treatment conditions as the CNC film samples. The compressive prestrain was released after corona treatment to induce a uniaxial compressive strain orthogonal to the prestrain direction on the surface of the PDMS, permanently wrinkling the corona treated thin film. AFM was then used to measure the wrinkle wavelength of the specimen (Figure S3) and calculate the effective thickness of the oxide layer required to decouple the modulus of the oxide from the modulus of the CNC films in the SIEBIMM experiments described here (Figure S4).

2.5 Optical microscopy

An inverted optical microscope (DMi-8, Leica Microsystems) equipped with cross polarizers was used to observe the birefringence of the CNC thin film and the wavelength of the film when compressed. A mechanical stage with two micrometers (Newport) was used to apply the incremental compressive strains to the specimen. The microscope was equipped with tile-mapping capabilities, allowing automated scans of the entire CNC film. The sequence of mapped images were assembled using the stitching function in ImageJ^[27] to produce composite images of the entire CNC film.

2.5.1 Birefringence microscopy

The polarizer and analyzer were adjusted to minimize the intensity of light detected from the microscope before placing the sample in the uniaxial micrometer stage. Once the sample was loaded, a tile map scan was captured and stitched.

2.5.2 **SIEBIMM** measurements

A tile map scan was collected of the unstrained sample, and sequential tile map scans of the entire film were captured at incremental displacement steps of $100 \, \mu m \, (0.4\% \, strain)$ until the entire film had reached the critical wrinkling strain. Each tile scan was compiled into an image stack such that consecutive images had increasing compressive strains. The stack was analyzed with a custom image analysis macro (MATLAB, MathWorks) to measure the wavelength of local positions, which is further discussed in the supplemental information. The wrinkle wavelength value taken at each position was recorded at or just beyond the critical wrinkling strain. This approach also allows the critical wrinkling strain as a function of CNC particle orientation and degree of alignment to be obtained spatially.

2.6 Coarse-grained modeling

2.6.1 Overview of CG model

Coarse-grained molecular dynamic (CG-MD) simulations have been used to systematically investigate the mechanical response of CNC thin films. [28] Within a validated 'bead-spring' CG model of CNC, 29 each CG bead corresponds to three repeat-units of the 36-chain structured (110) surface of $I\beta$ crystalline CNCs where the cross-section is 3.38 nm by 3.57 nm as described in further detail in previous studies. [30–32] The CG force field components include the contributions of the bonded and angular bending interactions along the axial direction of the fiber, which are captured by harmonic spring potentials and non-bonded pair interactions using the Morse potential.

This model is used as a theoretical reference point for the experimental results. More detailed information of the CG model development can be found in previous studies.^[30]

2.6.2 CG thin film modeling

CNC thin film systems with ordered and disordered CNCs were built to explore their mechanical behavior. Specifically, aligned CNCs were assembled into the simulation cell to form an anisotropic system comprised of 300 CNCs with 32 CG beads per CNC (with a length of approximately 100 nm), resulting in a film thickness of around 45 nm along the z-axis. To generate a representative disordered network, various numbers of CNCs, from 60 to 540 CNCs, with 32 CG beads per CNC were packed into a fixed simulation cell (150 nm by 150 nm by 45 nm), forming the randomly in-plane oriented configurations. Periodic boundary conditions (PBCs) were applied in the x-v plane and non-PBCs were applied in the z-direction to create free surfaces. Two perfectly smooth implicit walls were applied underneath and above the film to maintain the film geometry using a 9-3 Lennard Jones (LJ) potential. An integration timestep of $\Delta t = 5$ fs was adopted for all simulations. To equilibrate the system, the total potential energy was first minimized by using an iterative conjugate gradient algorithm. For a well-aligned CNC region, the CNC film underwent two annealing cycles from 1000 K to 300 K and was then equilibrated for another 10 ns at 300 K with zero pressure under isothermal-isobaric (NPT) ensemble; for disordered CNCs, the annealing cycle of simulation was carried out, followed by dynamics equilibration runs at the target density under the canonical (NVT) ensemble. Prior to deformation, structural stability and equilibration were confirmed by monitoring the total potential energy to ensure convergence. Large-scale Atomic/Molecular Massively Parallel Simulator (LAMMPS)[33] was used to implement all the MD simulations and the visualization of simulation snapshots was performed by Visual Molecular Dynamics (VMD).[34]

3. Results and Discussion

An advantage of this methodology is the spatial resolution enabled by the experimental design that can quantify the local CNC film modulus as a function of the radial and angular position. The radially aligned films are used to measure the film modulus of CNCs at various orientations relative to the compression direction through wrinkling as a function the position within the film. This technique is then used to describe the anisotropy of the local modulus of the thin film. Optical CNC orientation and surface buckling experimental results are then compared to mechanical modeling simulations that match the density of cellulose, film thicknesses, and CNC orientations using a coarse-grained (CG) model.

3.1 Birefringence

The diffraction of light passing through the CNC sample placed between two crossed polarizers is a function of the local refractive index of the film. In a radially aligned film, the difference between the refractive index in the transverse versus axial directions describes the birefringence of the film. Cross polarizers are used to observe birefringence and the degree of radial ordering of the CNCs within the film. A significant birefringent response (high contrast between orientation regions) suggests ordering. Previous work has shown that spin coated CNC films exhibit significant ordering from the analysis of refractive indices. [35] For the films produced in the present study, a Maltese cross, indicative of radial alignment, was observed during each birefringence experiment for the 40 nm, 70 nm, and 120 nm thick CNC films (Figure 2). The observation of a Maltese cross indicates a symmetry between the particles, however this characterization cannot identify if the film has radial or a Frank-Pryce structure. [36] Here, the presence of symmetry observed through birefringence is used as evidence of structure. The local variation in the moduli and its agreement with CG-MD results provide further evidence of radial alignment.

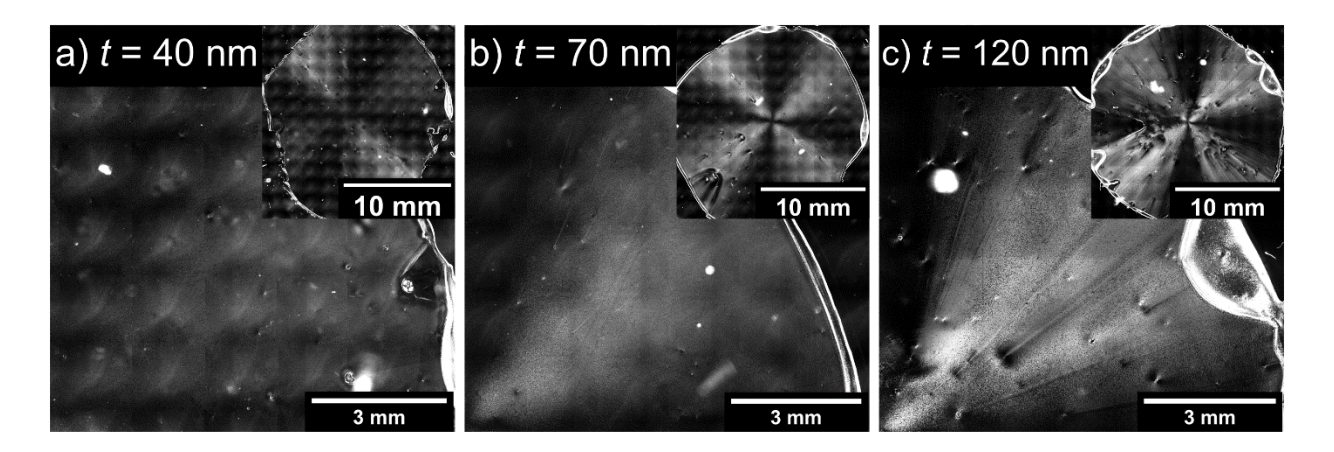


Figure 2: CNC films between two crossed polarizers for thicknesses of (a) 40 nm, (b) 70 nm, and (c) 120 nm. All three images have been modified in brightness and contrast to illustrate the birefringent response of the cellulose to indicate a radial orientation of CNC particles. Insets show the birefringence of the entire CNC film of r = 10 mm.

3.2 Modulus characterization

3.2.1 Wrinkle wavelength

The local wrinkling wavelength was measured across the sample at the onset of wrinkling. The larger tile map image (Figure 3) used for illustration purposes was obtained at a relatively high strain. In this macro image, the stiffer portions of the film (east and west poles, axially loaded CNCs) are well beyond their critical buckling strain and the more compliant regions of the film (north and south poles, transversely loaded CNCs) are just reaching their critical strain. This tile scan image taken near the end of an experiment is a good representation of how wrinkling begins and intensifies in regions of higher modulus first and then "fans out" as additional compressive strain is applied. The darker regions along the axially loaded CNCs show a higher contrast due to higher amplitudes from compressive strains that far exceed the critical wrinkling strains in those regions.

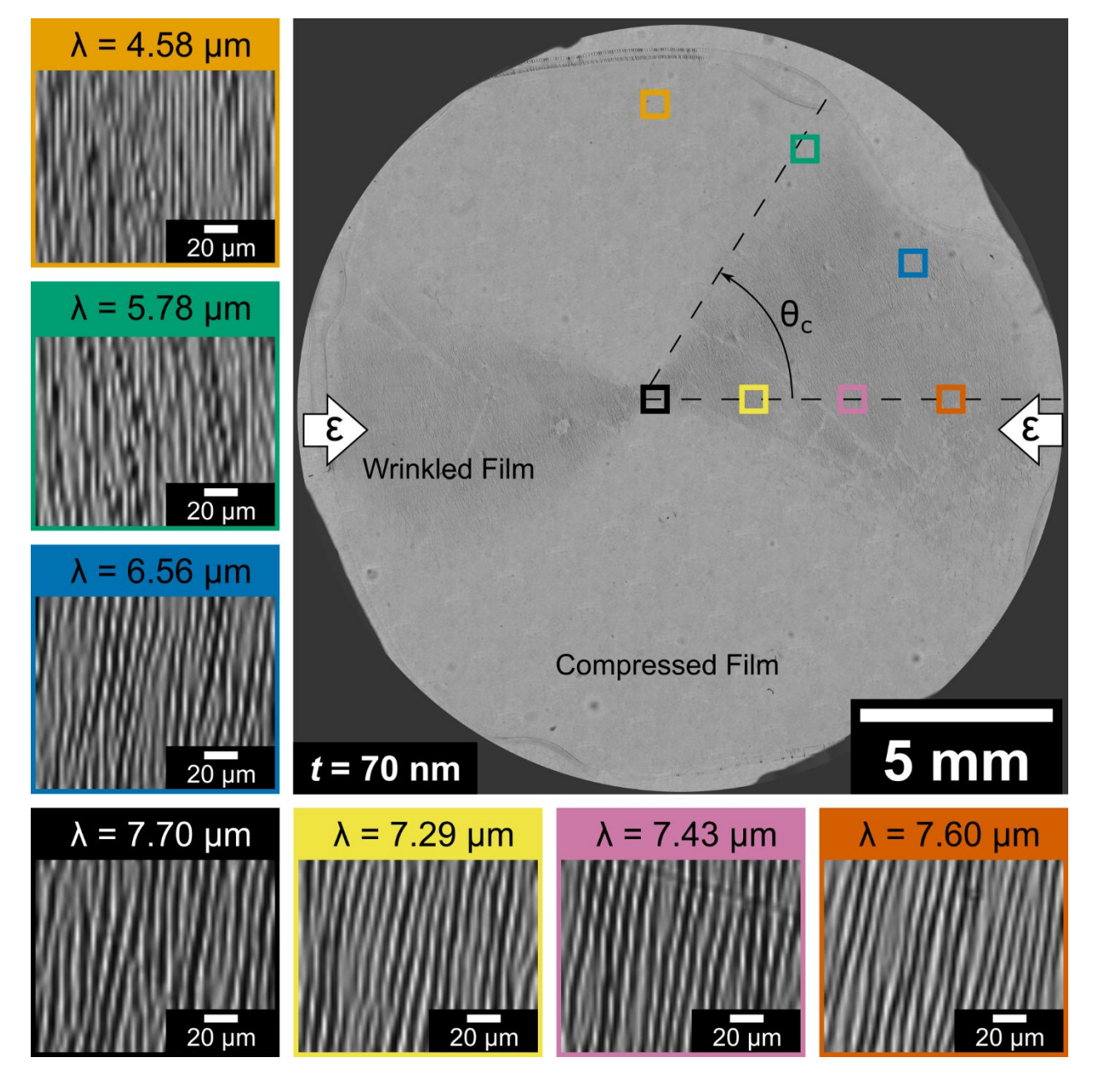


Figure 3: Wrinkle wavelength as a function of position on the film is angle dependent. Wavelength is greatest where particles are aligned in their axial direction (0° & 180°). Wavelength is lowest where particles are ordered in their transverse direction (90° & 270°). The transverse wavelength approaches 7.6 µm for the insets with increasing radius; conversely, the insets with increasing angle show a reduction in wavelength to a minimum of 4.58 µm.

At higher magnification, as shown in the images to the left and below the tile map, wrinkles can be observed at the critical wrinkling onset strain for each location. Each high magnification

image is color coded to indicate its location on the tile map. The effect of particle orientation on the wrinkle wavelength was clearly observed. For wrinkles formed from a compressive load applied in the same direction as the aligned CNCs (0 and 180°), the local wavelengths were relatively large, indicating a larger modulus along the CNC axes. Conversely, in the 90° and 270° positions, the wrinkling wavelength decreases because the compressive direction is oriented transverse to the CNC alignment direction. These results emphasize how a single wrinkling experiment can be used to measure the local CNC particle mechanics and extract the anisotropy of an anisotropic particle film under uniaxial compression.

The wrinkle wavelength, and thus CNC film modulus, had a slight dependence on position along the radius from the center to the edge of the film. This is because there was relatively little change in the shear forces experienced by the CNC suspension from the center towards the edge of the film. The particle alignment is assumed to be relatively constant as a function of radius because the whole oxidized region was quickly coated and dried during spincoating. Thus, we did not observe significant differences between the birefringence signal or measured modulus of the films in the radial direction.

3.2.2 Bilayer deconvolution

The corona treater was a useful processing tool for quickly depositing a hydrophilic oxide layer. [23,37] To account for the presence of an oxide layer between the CNC thin film and the PDMS, a bilayer thin film mechanics relationship was applied. This function determines the effective modulus ($E_{bilayer}$) based on the ratio of modulus values ($m = \frac{E_{CNC}}{E_{oxide}}$), the ratio of film thicknesses ($n = \frac{h_{CNC}}{h_{oxide}}$), the intermediate film modulus (E_{oxide}) and the surface film modulus (E_{CNC}). An illustration of the sample structure containing a bilayer film is further detailed in the supporting information.

$$E_{bilayer} = \frac{1 + m^2 n^4 + 2mn(2n^2 + 3n + 2)}{(1+n)^3 (1+mn)} E_{oxide}$$
 Equation (3)

Because the corona treatment on PDMS creates a thin oxide layer, the modulus was assumed to be equivalent to a glass film with a uniform modulus of 70 GPa through the thickness. [26] While it is likely that the oxide layer had a gradient modulus through the thickness, for the purpose of this approximation, it was taken as constant. The intermediate film (oxide) thickness of 3.1 nm was calculated using the oxide wrinkling wavelength of 560 nm observed via AFM. The thickness of the CNC film for each concentration was determined using an interferometer. By measuring the bilayer wavelength with the MATLAB script, an effective modulus was calculated, enabling the use of Equation 3 to determine the modulus of the CNC film.

3.2.3 Modulus mapping with orientation

The custom MATLAB script characterized local wavelengths of each strain step to map the change in modulus as a function of position across the film. The MATLAB code used thresholds to determine when each position had reached the critical wrinkling strain (onset of wrinkling) and used that slice to determine the wrinkle wavelength at that position. Thus, all of the wavelength values reported here were measured as close to the local critical onset strain as possible (within 0.4% strain). The wavelengths of the stiffest portions of the film (0°) were calculated from one of the earliest slices while those of the more compliant regions of the film (90°) were measured from further along in the sequential compressive loading experiment. Figure 4 compares the mapped results of two different film thicknesses (70 nm and 120 nm) and analyzes the modulus dependency on angle and radius. In Figure 4 (a & d), the film modulus up to a radius of 6.5 mm is mapped and plotted as a linearly interpolated contour plot. The CNC modulus calculated from Equation 3 is plotted beside the bilayer wavelength observed from optical microscopy to detail the scaling relationship from the bilayer film.

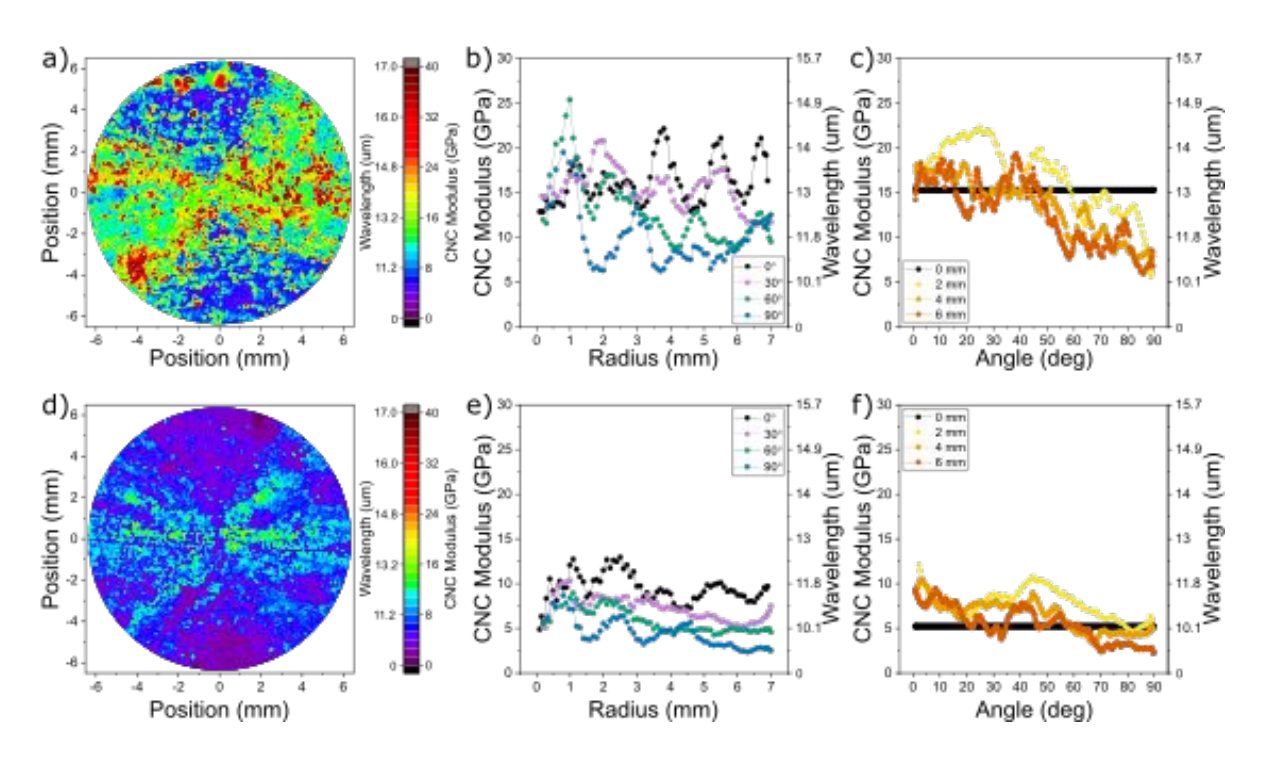


Figure 4: CNC film modulus values with film thicknesses of 70 and 120 nm were mapped using a custom MATLAB Script to measure local wavelengths. (a & d) The mapped images are illustrated for the 3 wt% concentration film (70 nm) and the 4 wt% concentration film (120 nm). The colorbar scales linearly with CNC modulus; the wavelength ticks are values corresponding to the respective CNC modulus value and do not share the same scaling. (b & e) The average of the four quadrants was plotted as a function of angle with a constant radius and (c & f) as a function of radius with a constant angle.

The global difference in modulus between the 70 nm and 120 nm mapped images is attributed to the effective number of CNC layers where the thickest films have too many interparticle interactions to act cooperatively and lose neat packing, but more data acquisition as a function of film thickness is needed to support this hypothesis. In Figure 4 (b & e), the CNC modulus for each angle loosely converges towards a different value. Each quadrant was overlayed and a moving average of three units was applied to remove noise. The pronounced oscillations in Figure 4 b for the 0 ° orientation are a result of image processing artifacts and are discussed in more detail in the Supporting Information. Progressing from a state of isotropy at the center of the

film to a higher degree of anisotropy at the edges of the film is indicative of an increasing degree of alignment.

The measured change in modulus as a function of angle can be observed in Figure 4 (c & f). The anisotropy of both CNC thin films is evident as the CNC modulus decreases from the axial orientation (0°) to the transverse orientation (90°). These results support our hypothesis of local stiffening due to radial alignment of the CNCs and are in good agreement with the results obtained from the CG-MD simulations. This method of local mapping of the film wrinkling behavior succinctly identifies the change in local modulus as a function of the degree of alignment of local CNC particles and the CNC particle orientation. One of the most significant contributions of this study is the methodology, which can be extended into other particle film systems as a wholistic measurement tool for determining modulus and anisotropy as a function of particle arrangement.

3.3 Simulation results

As shown in Figure 5a and 5b, CNC thin film systems with ordered and disordered CNCs were simulated to explore the structure-property relationships of their mechanical behavior. Specifically, a tensile loading with a strain rate of 0.05 ns⁻¹ was applied in the x-direction for an ordered region at 0°, in the x-y-direction with an orientation angle of 45°, and in the y-direction at 90°, which corresponded to the change in mechanical response with respect to the local directionality of the CNC particle orientation observed within the thin film (Figure 5a). From simulated tensile testing of the ordered CNC region, the elastic modulus was obtained from the stress versus strain curve as shown in Figure 5c, where the fluctuating red line shows the stress output for the orientation angle of 0° (right, y-axis) compared to the blue solid and dashed lines showing the results for the orientation angles of 45° and 90°, respectively (left, y-axis). The modulus was determined by fitting the stress-strain of the linear regime below a strain of 1% as

marked by the black dashed lines. The modulus in the axial loading direction (0°) was significantly greater than the modulus of the other two directions (45° & 90°) in addition to the fluctuating amplitude of stress in the strain hardening regime. These simulation results demonstrate that the mechanical responses of well-aligned CNCs under tension vary substantially with directionality of the nanostructure, which is consistent with the experimental measurements shown above. It should be noted that additional simulations with lower strain rates of 5e-3 ns⁻¹ and 5e-4 ns⁻¹ were also performed (see Figure S6 in Supporting Information) to explore possible strain rate effects, however, no significant rate dependence of modulus was observed.

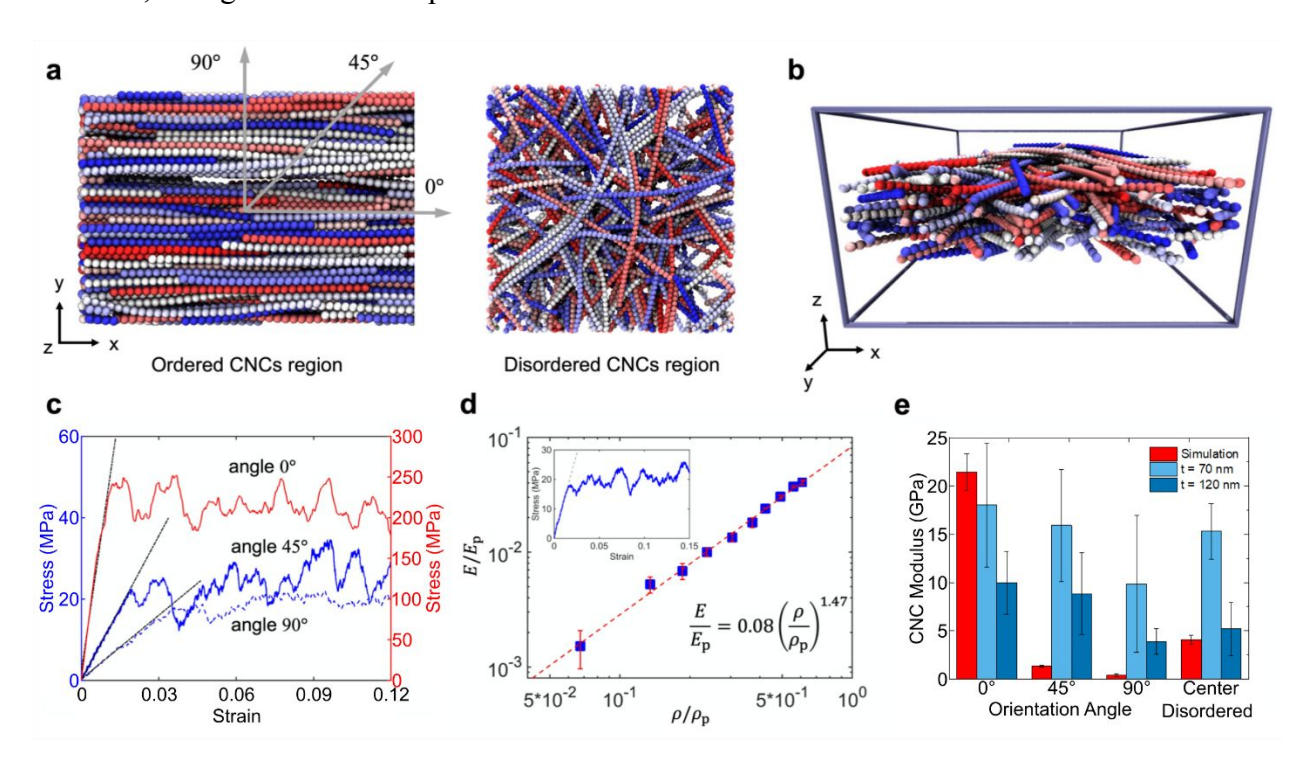


Figure 5: (a) Snapshots of the coarse-grained (CG) model of CNC films in the ordered and disordered regions, respectively (top view). (b) Snapshot of the simulation box with a disordered CNC film system consisting of several randomly oriented CG fibers (3D side view). (c) Representative stress-strain relation in three different loading directions in the ordered CNC region. (d) For the CNC region with random particle distribution, the power-law scaling relationship between normalized E/E_p and ρ/ρ_p , where $E_p = 134$ GPa and $\rho_p = 1.63$ g cm⁻³, corresponding to the Young's modulus and density of pristine or individual CNCs is shown. Inset shows the representative tensile stress-strain response of a CNC thin film in the disordered region. (e) Comparison of the experimental and simulated modulus results for the CNC films with different orientation and disordered configuration.

To gain better insights into highly disordered CNC regions, the influence of packing density on the modulus of CNC films having a porous network structure was investigated. Previous experimental and simulation studies have reported that both the modulus and strength of nanocellulose-based materials with porous structures exhibit a noticeable increase with density. [31,39] Experimentally, it is commonly observed that neat CNC films with higher porosity $(0.2 \text{ g cm}^{-3} < \rho < 0.9 \text{ g cm}^{-3})$ have typically been produced through solution casting techniques. [7] In the present simulations, the density of CNC films is varied from approximately 0.1 g cm⁻³ to 1.0 g cm⁻³ by adjusting the amount of CNCs contained in the simulation cell. The inset in Figure 5d shows the representative stress-strain output for the CNC network in the disordered region, which is characteristically similar to those for the well-aligned CNCs with orientation angles of 0° and 45°. Remarkably, there exists a scaling relationship between modulus and density normalized by the values of individual pristine I β CNC (i.e., ρ_p of 1.63 g cm⁻³ and E_p of 134 GPa), which can be described by the well-established power-law Gibson and Ashby (GA) model^[40] for foam-like porous systems: $E/E_p = C(\rho/\rho_p)^n$, where C and n are adjustable constants and ρ_p and E_p are the density and modulus of pristine CNCs given above.^[41,42] Experimentally, the value of n generally lies in the range from 1 to 4 based upon the specific microstructure of the cellular material, such that n = 2 for conventional polymeric open-cell foams and n = 2.73 for 3Dgraphene assemblies. [29,43] Consistent with this expected scaling relationship, the values of C and n are estimated to be 0.08 and 1.47, respectively, from our simulations (Figure 5d). Determining such scaling relationship values is useful in understanding the structure-property correlations of CNC thin films and in predicting the mechanical performance of the high-porosity film system with randomly oriented CNCs from a design perspective.

Figure 5e shows a comparison of the results of elastic moduli obtained from the experiment and simulations. For the well-aligned CNC regions, the moduli with varying orientation angles (i.e., 0°, 45°, and 90°) obtained from CG simulations are 21.4 GPa, 1.4 GPa, and 0.5 GPa, which are different but follow the same general trend as the values obtained from the experiments. For the central region where CNCs are randomly oriented in-plane, it is observed that the modulus of 4.1 GPa of the film with $\rho \approx 0.8$ g cm⁻³ (similar to the estimated density of the well-aligned CNC films) from the simulations based on the power-law scaling relationship is lower than the experimental measurement. Despite the difference in the magnitudes of CNC thin film moduli, the simulation trend is in qualitative agreement with the experimental observations: $E(0^{\circ}) > E(\text{center})$ or disordered) $\sim E(45^{\circ}) > E(90^{\circ})$, corroborating the finding that the modulus varies significantly with respect to directionality and ordering of CNCs in thin film systems. The deviation of the simulated E values from the experimental measurement might be attributed to several factors, such as idealization of the CNC model that has uniform distribution in length and cross-section dimension, inconsistency of film density in the experimental specimens which highly affects the modulus, as well as the microstructural difference associated with packing and orientation of CNCs. Regardless, the results obtained from CG-MD simulations, in general, agree well with the trend identified from the experimental observations, demonstrating the important role of CNC orientation and microstructure in the mechanical response of thin films.

4. Conclusion

Using spin coating to deposit a radially aligned CNC thin film, the modulus and anisotropy of a CNC thin film were characterized using SIEBIMM as a function of local orientation and degree of alignment of CNC particles. The results concluded that a high degree of alignment of the particles led to significant anisotropy in the axial and transverse moduli of the CNC thin films.

Additionally, the modulus was highly dependent on the local particle orientation relative to the compressive direction. This approach can be extended to high aspect ratio particle thin film assemblies to characterize modulus and anisotropy in a succinct methodology using buckling instabilities. Future work will focus on the influence of film thickness on the ordering and anisotropic mechanical response of CNC particle films. This method is both wholistic and detailed for describing mechanical properties with multiple metrics of measurement: birefringence microscopy for measuring through-thickness degree of alignment, strain-induced instability characterization for modulus measurement, and strain-step imaging for characterizing the onset of critical strain.

Supporting Information: Explanation of indentation measurements of substrate modulus. Static water contact angles before and after corona treatment. Bilayer deconvolution and determination of oxide layer thickness. Description of MATLAB code. Microscopy images of 40nm CNC film. CG-MD strain rate effect results.

Acknowledgements

N.M. and C.D. thank R. Plotner for contact angle imaging, J. Blendell and K. Yazawa for AFM training and assistance, J. Youngblood for supplying the CNC suspension, the Office of Undergraduate Research (OUR) at Purdue University for funding the research, and Purdue University. Z.L. and W.X. acknowledge the support from the National Science Foundation (NSF) under NSF CMMI Award No. 2113558 and North Dakota State University (NDSU) Foundation and Alumni Association through the Centennial Endowment Fund. This work used supercomputing resources of the CCAST at NDSU, which were made possible in part by NSF MRI Award No. 2019077.

References

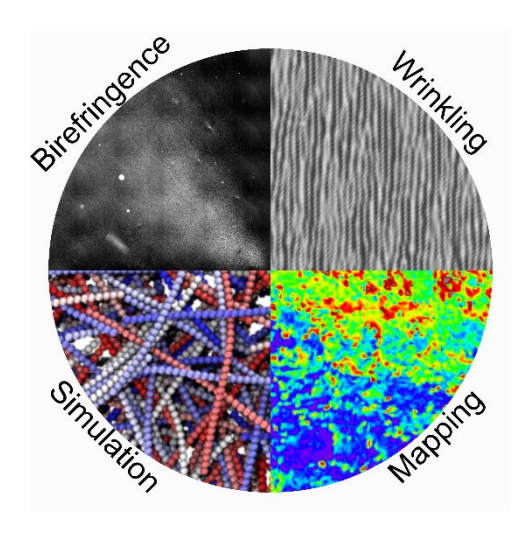
- (1) Habibi, Y.; Lucia, L. A.; Rojas, O. J. Cellulose Nanocrystals: Chemistry, Self-Assembly, and Applications. *Chem. Rev.* **2010**, *110* (6), 3479–3500. https://doi.org/10.1021/cr900339w.
- (2) Parker, R. M.; Guidetti, G.; Williams, C. A.; Zhao, T.; Narkevicius, A.; Vignolini, S.; Frka-Petesic, B. The Self-Assembly of Cellulose Nanocrystals: Hierarchical Design of Visual Appearance. *Adv. Mater.* **2018**, *30* (19). https://doi.org/10.1002/adma.201704477.
- (3) Prishchepa, O. O.; Zyryanov, V. Y.; Gardymova, A. P.; Shabanov, V. F. Optical Textures and Orientational Structures of Nematic and Cholesteric Droplets with Heterogeneous Boundary Conditions. *Mol. Cryst. Liq. Cryst.* **2008**, *489* (April), 84–93. https://doi.org/10.1080/15421400802219817.
- (4) Gençer, A.; Schütz, C.; Thielemans, W. Influence of the Particle Concentration and Marangoni Flow on the Formation of Cellulose Nanocrystal Films. *Langmuir* **2017**, *33* (1), 228–234. https://doi.org/10.1021/acs.langmuir.6b03724.
- (5) Csoka, L.; Hoeger, I. C.; Rojas, O. J.; Peszlen, I.; Pawlak, J. J.; Peralta, P. N. Piezoelectric Effect of Cellulose Nanocrystals Thin Films. *ACS Macro Lett.* **2012**, *1* (7), 867–870. https://doi.org/10.1021/mz300234a.
- (6) Song, W.; Lee, J. K.; Gong, M. S.; Heo, K.; Chung, W. J.; Lee, B. Y. Cellulose Nanocrystal-Based Colored Thin Films for Colorimetric Detection of Aldehyde Gases. *ACS Appl. Mater. Interfaces* **2018**, *10* (12), 10353–10361. https://doi.org/10.1021/acsami.7b19738.
- (7) Moon, R. J.; Martini, A.; Nairn, J.; Simonsen, J.; Youngblood, J. P. Cellulose Nanomaterials Review: Structure, Properties and Nanocomposites. *Chem. Soc. Rev.* **2011**, *40* (7), 3941–3994. https://doi.org/10.1039/c0cs00108b.
- (8) Garcia de Rodriguez, N. L.; Thielemans, W.; Dufresne, A. Sisal Cellulose Whiskers Reinforced Polyvinyl Acetate Nanocomposites. *Cellulose* **2006**, *13* (3), 261–270. https://doi.org/10.1007/s10570-005-9039-7.
- (9) Lahiji, R. R.; Xu, X.; Reifenberger, R.; Raman, A.; Rudie, A.; Moon, R. J. Atomic Force Microscopy Characterization of Cellulose Nanocrystals. *Langmuir* **2010**, *26* (6), 4480–4488. https://doi.org/10.1021/la903111j.
- (10) Tashiro, K.; Kobayashi, M. Theoretical Evaluation of Three-Dimensional Elastic Constants of Native and Regenerated Celluloses: Role of Hydrogen Bonds. *Polymer.* **1991**, *32* (8), 1516–1526. https://doi.org/10.1016/0032-3861(91)90435-L.
- (11) Gardner, D. J.; Oporto, G. S.; Mills, R.; Samir, M. A. S. A. Adhesion and Surface Issues in Cellulose and Nanocellulose. *J. Adhes. Sci. Technol.* **2008**, *22* (5–6), 545–567. https://doi.org/10.1163/156856108X295509.

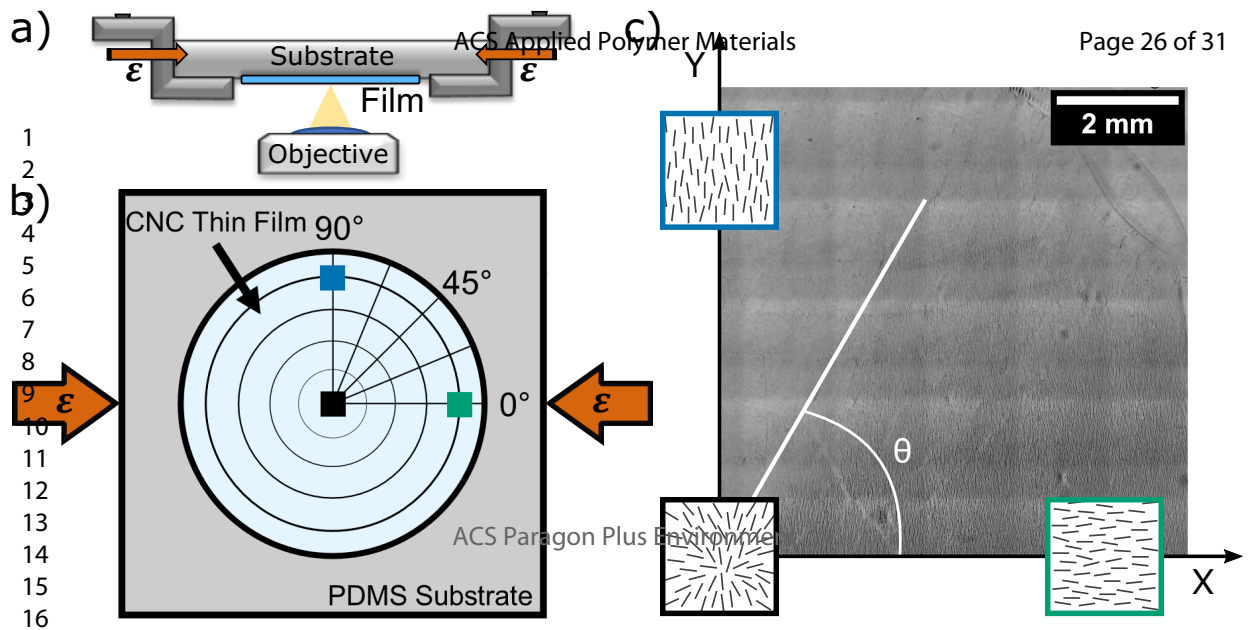
- (12) Wang, H.; He, J.; Zhang, M.; Tam, K. C.; Ni, P. A New Pathway towards Polymer Modified Cellulose Nanocrystals via a "Grafting onto" Process for Drug Delivery. *Polym. Chem.* **2015**, *6* (23), 4206–4209. https://doi.org/10.1039/c5py00466g.
- (13) Reising, A. B.; Moon, R. J.; Youngblood, J. P. Effect of Particle Alignment on Mechanical Properties of Neat Cellulose Nanocrystal Films. *J-for-Journal Sci. Technol. For. Prod. Process.* **2012**, *2* (6), 32–41.
- (14) Cranston, E. D.; Eita, M.; Johansson, E.; Netrval, J.; Salajková, M.; Arwin, H.; Wagberg, L. Determination of Young's Modulus for Nanofibrillated Cellulose Multilayer Thin Films Using Buckling Mechanics. *Biomacromolecules* **2011**, *12* (4), 961–969. https://doi.org/10.1021/bm101330w.
- (15) Kan, K. H. M.; Cranston, E. D. Mechanical Testing of Thin Film Nanocellulose Composites Using Buckling Mechanics. *TAPPI J.* **2013**, *12* (4), 35–43.
- (16) Stafford, C. M.; Vogt, B. D.; Harrison, C.; Julthongpiput, D.; Huang, R. Elastic Moduli of Ultrathin Amorphous Polymer Films. *Macromolecules* **2006**, *39* (15), 5095–5099. https://doi.org/10.1021/ma060790i.
- (17) Stafford, C. M.; Harrison, C.; Beers, K. L.; Karim, A.; Amis, E. J.; Vanlandingham, M. R.; Kim, H.-C. C.; Volksen, W.; Miller, R. D.; Simonyi, E. E. A Buckling-Based Metrology for Measuring the Elastic Moduli of Polymeric Thin Films. *Nat. Mater.* **2004**, *3* (8), 545–550. https://doi.org/10.1038/nmat1175.
- (18) Lagerwall, J. P. F.; Schütz, C.; Salajkova, M.; Noh, J.; Park, J. H.; Scalia, G.; Bergström, L. Cellulose Nanocrystal-Based Materials: From Liquid Crystal Self-Assembly and Glass Formation to Multifunctional Thin Films. *NPG Asia Mater.* **2014**, *6* (1), 1–12. https://doi.org/10.1038/am.2013.69.
- (19) Hewson, D.; Vukusic, P.; Eichhorn, S. J. Reflection of Circularly Polarized Light and the Effect of Particle Distribution on Circular Dichroism in Evaporation Induced Self-Assembled Cellulose Nanocrystal Thin Films. *AIP Adv.* **2017**, 7 (6). https://doi.org/10.1063/1.4986761.
- (20) Jiang, M.; Demass, S. N.; Economy, D. R.; Shackleton, T.; Kitchens, C. L. Formation of Highly Oriented Cellulose Nanocrystal Films by Spin Coating Film from Aqueous Suspensions. *J. Renew. Mater.* **2016**, *4* (5), 377–387. https://doi.org/10.7569/JRM.2016.634131.
- (21) Son, H.; Chau, A. L.; Davis, C. S. Polymer Thin Film Adhesion Utilizing the Transition from Surface Wrinkling to Delamination. *Soft Matter* **2019**, *15* (31). https://doi.org/10.1039/C9SM01052A.
- (22) Johnston, I. D.; McCluskey, D. K.; Tan, C. K. L.; Tracey, M. C. Mechanical Characterization of Bulk Sylgard 184 for Microfluidics and Microengineering. *J. Micromechanics Microengineering* **2014**, *24* (3), 035017. https://doi.org/10.1088/0960-1317/24/3/035017.

- (23) Haubert, K.; Drier, T.; Beebe, D. PDMS Bonding by Means of a Portable, Low-Cost Corona System. *Lab Chip* **2006**, *6* (12), 1548–1549. https://doi.org/10.1039/b610567j.
- (24) Morra, M.; Occhiello, E.; Marola, R.; Garbassi, F.; Humphrey, P.; Johnson, D. On the Aging of Oxygen Plasma-Treated Polydimethylsiloxane Surfaces. *J. Colloid Interface Sci.* **1990**, *137*, 11–24. https://doi.org/10.1016/0021-9797(90)90038-P.
- (25) Deagen, M. E.; Chan, E. P.; Schadler, L. S.; Ullal, C. K. Corona Treatment for Nanotransfer Molding Adhesion. *ACS Appl. Polym. Mater.* **2019**, *1* (5), 997–1005. https://doi.org/10.1021/acsapm.9b00028.
- (26) Bowden, N.; Huck, W. T. S. S.; Paul, K. E.; Whitesides, G. M. The Controlled Formation of Ordered, Sinusoidal Structures by Plasma Oxidation of an Elastomeric Polymer. *Appl. Phys. Lett.* **1999**, *75* (17), 2557. https://doi.org/10.1063/1.125076.
- (27) Preibisch, S.; Saalfeld, S.; Tomancak, P. Globally Optimal Stitching of Tiled 3D Microscopic Image Acquisitions. *Bioinformatics* **2009**, *25* (11), 1463–1465. https://doi.org/10.1093/bioinformatics/btp184.
- (28) Ramezani, M. G.; Golchinfar, B. Mechanical Properties of Cellulose Nanocrystal (CNC) Bundles: Coarse-Grained Molecular Dynamic Simulation. *J. Compos. Sci.* **2019**, *3* (2), 1–13. https://doi.org/10.3390/jcs3020057.
- (29) Qin, Z.; Jung, G. S.; Kang, M. J.; Buehler, M. J. The Mechanics and Design of a Lightweight Three-Dimensional Graphene Assembly. *Sci. Adv.* **2017**, *3* (1), e1601536. https://doi.org/10.1126/sciadv.1601536.
- (30) Qin, X.; Feng, S.; Meng, Z.; Keten, S. Optimizing the Mechanical Properties of Cellulose Nanopaper through Surface Energy and Critical Length Scale Considerations. *Cellulose* **2017**, *24* (8), 3289–3299. https://doi.org/10.1007/s10570-017-1367-x.
- (31) Li, Z.; Xia, W. Coarse-Grained Modeling of Nanocellulose Network towards Understanding the Mechanical Performance. *Extrem. Mech. Lett.* **2020**, *40*, 100942. https://doi.org/10.1016/j.eml.2020.100942.
- (32) Li, Z.; Liao, Y.; Zhang, Y.; Zhang, Y.; Xia, W. Microstructure and Dynamics of Nanocellulose Films: Insights into the Deformational Behavior. *Extrem. Mech. Lett.* **2022**, *50*, 101519. https://doi.org/10.1016/j.eml.2021.101519.
- (33) Plimpton, S. Fast Parallel Algorithms for Short-Range Molecular Dynamics. *J. Comput. Phys.* **1995**, *117*, 1–19.
- (34) Humphrey, W.; Dalke, A.; Schulten, K. VMD: Visual Molecular Dynamics. *J. Mol. Graph.* **1996**, *14* (1), 33–38. https://doi.org/10.1016/0263-7855(96)00018-5.
- (35) Cranston, E. D.; Gray, D. G. Birefringence in Spin-Coated Films Containing Cellulose Nanocrystals. *Colloids Surfaces A Physicochem. Eng. Asp.* **2008**, *325* (1–2), 44–51. https://doi.org/10.1016/j.colsurfa.2008.04.042.

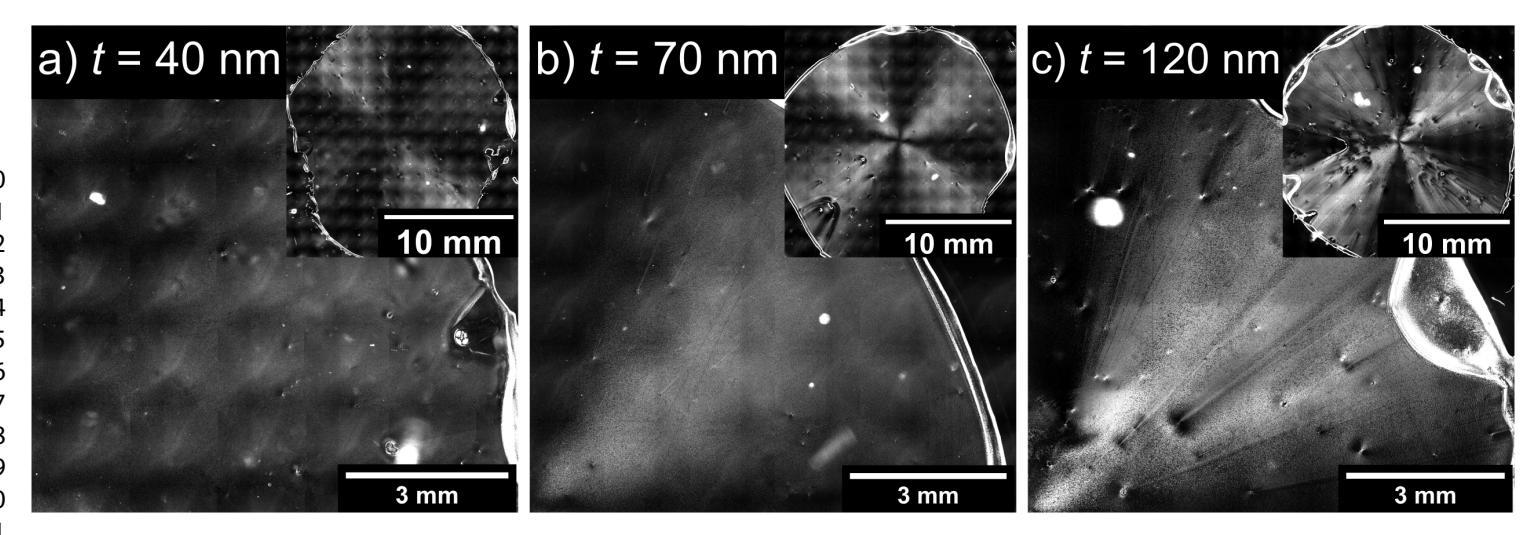
- (36) Bajc, J.; Crooker, P. P.; Zumer, S. Chiral Nematic Liquid Crystal Droplets. *Liq. Cryst. Today* **1997**, *7* (3), 1–6. https://doi.org/10.1080/13583149708047675.
- (37) Nania, M.; Matar, O. K.; Cabral, J. T. Frontal Vitrification of PDMS Using Air Plasma and Consequences for Surface Wrinkling. *Soft Matter* **2015**, *11* (15), 3067–3075. https://doi.org/10.1039/c4sm02840f.
- (38) Stafford, C. M.; Guo, S.; Harrison, C.; Chiang, M. Y. M. Combinatorial and High-Throughput Measurements of the Modulus of Thin Polymer Films. *Rev. Sci. Instrum.* **2005**, 76 (6). https://doi.org/10.1063/1.1906085.
- (39) Henriksson, M.; Berglund, L. A.; Isaksson, P.; Lindström, T.; Nishino, T. Cellulose Nanopaper Structures of High Toughness. *Biomacromolecules* **2008**, *9* (6), 1579–1585. https://doi.org/10.1021/bm800038n.
- (40) Gibson, I. J.; Ashby, M. F. The Mechanics of Three-Dimensional Cellular Materials. *Proc. R. Soc. London. A. Math. Phys. Sci.* **1982**, 382 (1782), 43–59. https://doi.org/10.1098/rspa.1982.0088.
- (41) Brezny, R.; Green, D. J. The Effect of Cell Size on the Mechanical Behavior of Cellular Materials. *Acta Metall. Mater.* 1990, 38 (12), 2517–2526. https://doi.org/10.1016/0956-7151(90)90263-G.
- (42) Istrate, O. M.; Chen, B. Relative Modulus–Relative Density Relationships in Low Density Polymer–Clay Nanocomposite Foams. *Soft Matter* **2011**, *7* (5), 1840–1848. https://doi.org/10.1039/C0SM01052A.
- (43) Roberts, A. P.; Garboczi, E. J. Elastic Properties of Model Random Three-Dimensional Open-Cell Solids. *J. Mech. Phys. Solids* **2002**, *50* (1), 33–55. https://doi.org/10.1016/S0022-5096(01)00056-4.

TOC Graphic

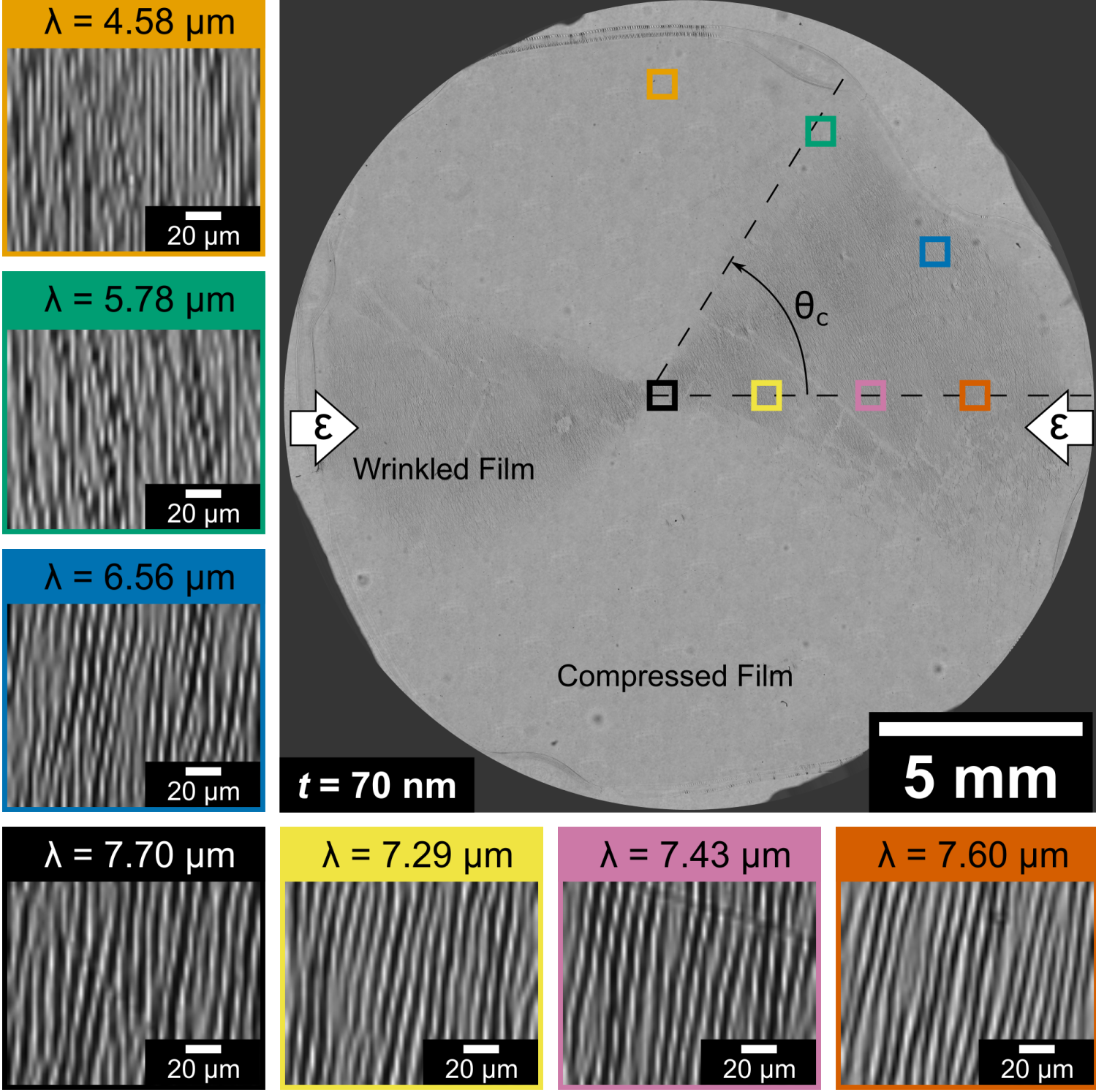




Miller et al Fig 2.pdf 2589 x 866





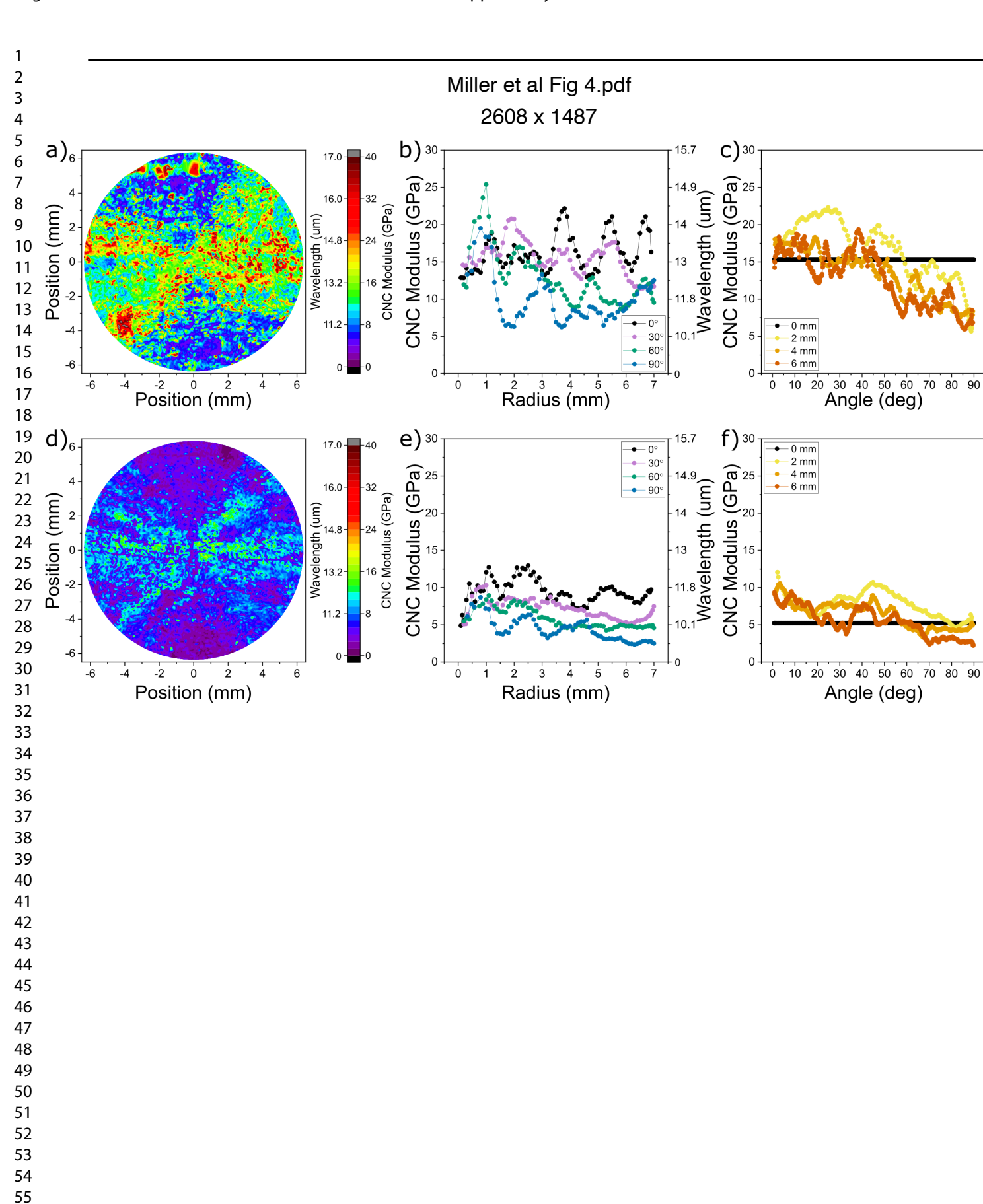


15.7

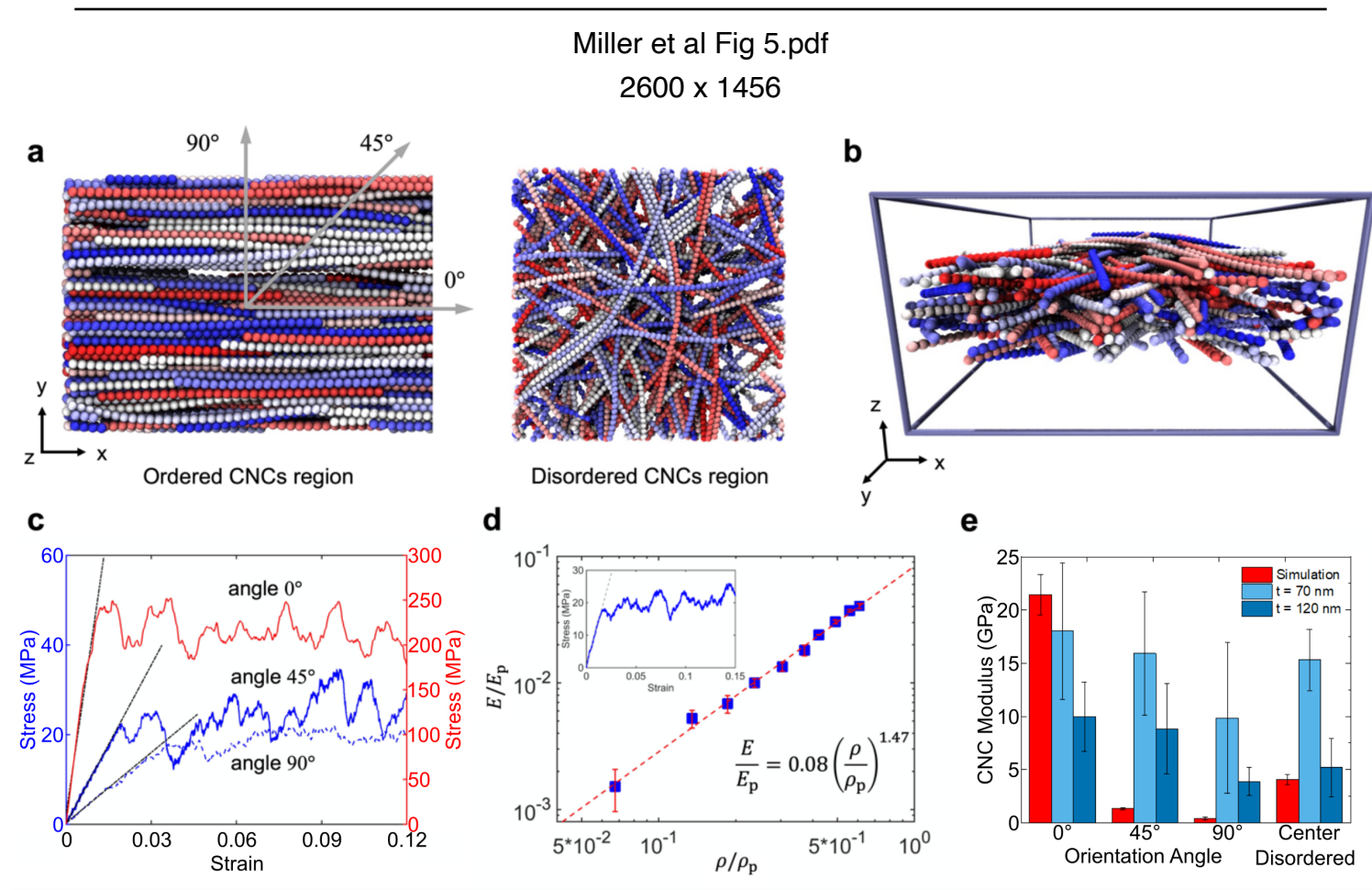
15.7

Wavelength (um

60



Page 30 of 31



Miller et al TOC Graphic.pdf 2600 x 2600

